Beamforming and Its Applications to Brain Connectivity

Armin Fuchs

Center for Complex Systems & Brain Sciences, Department of Physics,
Florida Atlantic University, Boca Raton, FL 33487
fuchs@ccs.fau.edu

In this chapter we show how beamforming, an analysis procedure for EEG and MEG data sets that is becoming increasingly popular, can be used to obtain insight about functional connectivity between brain regions. To this end we introduce a parameterization of cortical surfaces based on output from the software package *Freesurfer* and restrict the potential current sources to the cortical gray matter. We create a data set assuming two brain areas being active with different time dependencies of the activation. These activation patterns are then reconstructed using beamforming procedures with a variety of parameters demonstrating the dependencies of the reconstructed patters of activity on these parameters. Finally, we apply two statistical techniques, namely coherence and Granger causality to the data set, showing that the data can be understood by assuming a one-directional connection between the two active brain regions.

1 Introduction

In recent years an analysis procedure called beamforming has become increasingly popular for the analysis of non-invasively recorded electrophysiological data sets like EEG (electroencephalogram) and MEG (magnetoencephalogram). The original ideas can be found in the engineering literature of the 1970's [1], [2] (see also [3]) before they were applied to brain imaging roughly 25 years later [4], [5], [6]. The goal of beamforming is to use an array of sensors and combine the signals recorded at individual sites to increase the signal/noise ratio or resolution, and to focus the entire array on a certain region in space. The best known example for this technique is found in astronomy where many radio telescopes that can be distributed all over the earth behave as a virtual single antenna. In brain imaging, arrays of up to about 250 electrodes (EEG) or SQuID (superconducting quantum interference device) sensors (MEG) are used to measure the electric potential on the scalp surface or the tiny magnetic fields produced by the electric currents flowing inside

the brain, respectively. When beamforming is applied to electrophysiological recordings the intention is to find the magnitudes, locations and directions of these currents, in short, detect the neurally active regions of the brain under a certain task. Various flavors of beamforming algorithms can be found in the literature and we will discuss their similarities and differences later in this chapter. In most applications beamformers are used to scan regions of interest or the entire brain volume on a voxel by voxel basis [4], [5], [6]. More recently a slightly different approach has been developed which applies anatomical constraints to the locations and directions of potential cortical sources [7], [8]. Specifically, the locations of neural activity are restricted to the cortical gray matter and the directions of the currents are assumed to be perpendicular to the cortical surface. The reasons for these constraints on location and direction are twofold: first, in the cortical gray matter pyramidal cells form columns which are orthogonal to the folded surface and the current flow is along these columns [9]. Second, the columns are bundled together to form so-called macrocolumns of about 10^5 neurons acting coherently [10]. It has been estimated that several tens of thousands of simultaneously active cells are necessary to produce a signal that can be picked up by EEG or MEG [11] and the only part of the brain where this is the case is the cortical gray matter[1].

We will proceed through this chapter in four steps: first, we will show how MRI scans and the locations of sensors of a magnetometer used to record MEG can be coregistered to a common coordinate system, and how the cortical surfaces can be extracted and parameterized. Second, we will create a dataset by assuming neural activity in two distinct regions along opposite walls of the central sulcus and calculate the spatiotemporal patterns that would be measured by the MEG system. Third, we will use this dataset and apply beamformers to reconstruct the activity in order to show how certain parameters affect the quality of performance. Finally, fourth, we will demonstrate how the statistical measures known as coherence and Granger causality allow us to identify functional connectivity between brain regions including the direction of influence between different locations on the cortical surface.

2 Coregistration and Parameterization of Cortical Surfaces

In order to combine the recordings from different imaging modalities it is necessary to represent all data in a common coordinate system. This sounds like a trivial prerequisite but the different manufacturers of EEG and MEG recording systems all have their specific preferences and a commonly accepted

[1] An exception to this rule is the auditory brainstem response but in this case several thousand events have to be averaged in order to obtain a decent signal/noise ratio.

standard is nowhere in sight. Moreover, radiologists like to display the patient's left side on the right and vice versa, because this is the view they get when they look at them face to face.

2.1 Coregistration

The coordinate system we will use here is based on three landmarks on the human head that can easily be identified: the left and right pre-auricular points and the nasion. Our x-axis runs from the left to the right pre-auricular point, the y-axis runs through the nasion and has an intersection with the x-axis at a right angle. The z-axis is orthogonal to the xy-plane through the origin and points upwards to form a right-handed coordinate system. In a first step we will transform a structural MRI scan and the locations of EEG electrodes and MEG sensors into these coordinates.

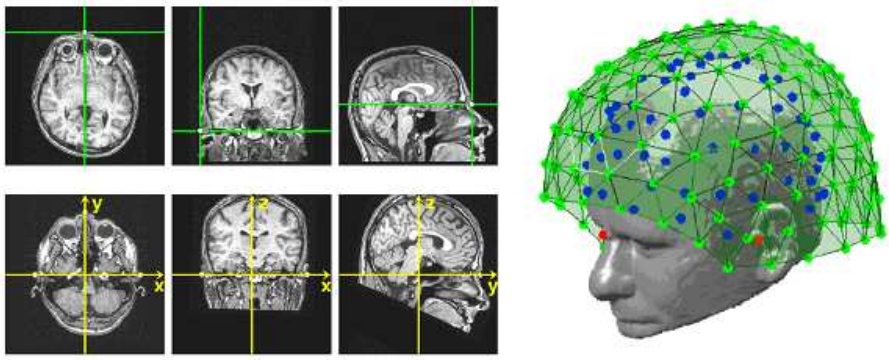

Fig. 1. Left top: Locations of fiducial points in a T_1 weighted fullhead MRI scan. Left bottom: The transformed volume. Note that all three landmarks are now located in the same axial slice, which represents the xy-plane. Right: The skin surface reconstructed from the MRI with fiducials (rod dots), EEG electrode locations (blue dots) and the surface defined by the locations of the MEG sensors (green).

Our starting point is a MRI volume of axial slices from a fullhead scan with a voxel size of $1 \times 1 \times 1\, mm^3$. From this scan the 3d-coordinates of three landmarks on the subject's head, i.e. the nasion and the left and right pre-auricular points, have to be found. This task is considerably simplified if vitamin E capsules have been attached to these points prior to the scan so that they can be easily identified as bright spots on a T_1 weighted scan due to the short spin-lattice relaxation time in its C-H_2 chains. The top row of fig. 1 (left) shows examples for such landmarks in an axial, coronal and sagittal slice, respectively. In these images no two of the fiducials are located in the same slice. Our goal is to find a transformation matrix that defines a rotation

and shift of the volume in 3d-space such that all three landmarks end up in the same axial slice which then defines the new xy-plane.

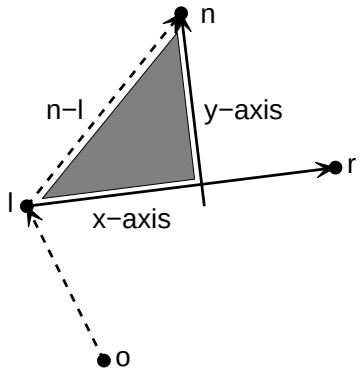

Fig. 2. Relation between the origin of the old coordinate system ($\boldsymbol{o}$), the landmarks ($\boldsymbol{l}$, $\boldsymbol{r}$ and $\boldsymbol{n}$) and the new x- and y-axis. The shaded triangle represents the vector relation (3).

Figure 2 shows a sketch of the relation between the landmarks ($\boldsymbol{r}$, $\boldsymbol{l}$, $\boldsymbol{n}$) and the old origin ($\boldsymbol{o}$). The new x-axis which runs from the left to the right pre-auricular is given by $\boldsymbol{l} + \alpha\,(\boldsymbol{r} - \boldsymbol{l})$. In the same way the xy-plane can be expressed as $\boldsymbol{l} + \gamma\,(\boldsymbol{r} - \boldsymbol{l}) + \beta\,(\boldsymbol{n} - \boldsymbol{l})$, where α, β and γ are arbitrary real numbers. The new y-axis is represented by the line in the xy-plane which is orthogonal to the x-axis and runs through the nasion ($\boldsymbol{n}$). All lines in the xy-plane perpendicular to the x-axis fulfill the condition

$$\{\gamma\,(\boldsymbol{r} - \boldsymbol{l}) + \beta\,(\boldsymbol{n} - \boldsymbol{l})\} \cdot \{\boldsymbol{r} - \boldsymbol{l}\} = 0 \tag{1}$$

which leads to a relation between γ and β, namely

$$\gamma = -\beta\,\frac{(\boldsymbol{n} - \boldsymbol{l}) \cdot (\boldsymbol{r} - \boldsymbol{l})}{|\,\boldsymbol{r} - \boldsymbol{l}\,|^2} \tag{2}$$

Using (2), the expression for the xy-plane and the abbreviations $\boldsymbol{r} - \boldsymbol{l} = \boldsymbol{r_l}$ and $\boldsymbol{n} - \boldsymbol{l} = \boldsymbol{n_l}$ the boundary of the shaded triangle in fig. 2 can be expressed as

$$\alpha\,\boldsymbol{r_l} + \beta\,\{\boldsymbol{n_l} - \frac{\boldsymbol{n_l} \cdot \boldsymbol{r_l}}{|\,\boldsymbol{r_l}\,|^2}\,\boldsymbol{r_l}\} = \boldsymbol{n_l} \tag{3}$$

representing a set of three linear equations for the three vector components, and α and β can readily be calculated from any two of them. The origin of the new coordinate system is then given by $\boldsymbol{l} + \alpha\boldsymbol{r_l}$, for instance. The directions of the new axes can be written in the form

$$\begin{aligned} \boldsymbol{r_l} & \quad \text{for the } x\text{-axis,} \\ \boldsymbol{n_l} - \tfrac{\boldsymbol{n_l}\cdot\boldsymbol{r_l}}{|\boldsymbol{r_l}|^2}\,\boldsymbol{r_l} & \quad \text{for the } y\text{-axis, and} \\ \boldsymbol{r_l} \times \{\boldsymbol{n_l} - \tfrac{\boldsymbol{n_l}\cdot\boldsymbol{r_l}}{|\boldsymbol{r_l}|^2}\,\boldsymbol{r_l}\} & \quad \text{for the } z\text{-axis.} \end{aligned} \tag{4}$$

Once normalized, these vectors compose the rotation matrix $\boldsymbol{R}$ which defines the new coordinate systems after the origin has been shifted to its new location $\boldsymbol{l} + \alpha\boldsymbol{r_l}$.

In general, a rotation in three dimensional space can be described by consecutive rotations around three axes and parameterized by the Euler angles ϕ, θ and ψ. There are various ways to define these angles and the sequence of rotations. We will use here a form that first rotates the volume around the z-axis, then around the y-axis and finally around the x-axis. The corresponding transformation matrix $\boldsymbol{R}$ is the product of the matrices that describe the single rotations and reads explicitly

$$\begin{aligned} \boldsymbol{R} = \boldsymbol{R_x}\boldsymbol{R_y}\boldsymbol{R_z} &= \begin{pmatrix} 1 & 0 & 0 \\ 0 & \cos\psi & \sin\psi \\ 0 & -\sin\psi & \cos\psi \end{pmatrix} \begin{pmatrix} \cos\theta & 0 & -\sin\theta \\ 0 & 1 & 0 \\ \sin\theta & 0 & \cos\theta \end{pmatrix} \begin{pmatrix} \cos\phi & \sin\phi & 0 \\ -\sin\phi & \cos\phi & 0 \\ 0 & 0 & 1 \end{pmatrix} \\ &= \begin{pmatrix} \cos\theta\cos\phi & \cos\theta\sin\phi & -\sin\theta \\ \sin\psi\sin\theta\cos\phi - \cos\psi\sin\phi & \sin\psi\sin\theta\sin\phi + \cos\psi\cos\phi & \sin\psi\cos\theta \\ \cos\psi\sin\theta\cos\phi + \sin\psi\sin\phi & \cos\psi\sin\theta\sin\phi - \sin\psi\cos\phi & \cos\psi\cos\theta \end{pmatrix} \end{aligned} \tag{5}$$

From the components R_{ij} of the rotation matrix on the right hand side of (5) we can determine the Euler angles as

$$\phi = \arctan\frac{R_{12}}{R_{11}} \qquad \theta = \arctan\frac{-R_{13}\sin\phi}{R_{12}} \qquad \psi = \arctan\frac{R_{23}}{R_{33}} \tag{6}$$

These angles together with the shift of the origin can be used in standard MRI software to create a new volume which has all three landmarks in the slice that now represents the xy-plane as shown in the bottom row of fig. 1 (left).

Transforming the locations of electrodes or sensors into the the same coordinate system is straightforward. First the new origin is calculated according to (3) and the locations are shifted. Then a rotation with the normalized matrix (4) is performed which completes the coregistration procedure between the subject's head, and the electrodes and sensors as shown in fig. 1 (right).

2.2 Parameterizing the Folded Brain Surfaces

The work of Dale, Sereno, Fischl and co-workers provided the scientific community with a powerful software tool known as *Freesurfer* [17], [18], [19]. Freesurfer creates tessellations of cortical surfaces like the boundary between the gray and white matter or the boundary between the gray matter and the

cerebral spinal fluid. The folded surfaces for each hemisphere can then be inflated by reducing the local curvature in an iterative process and eventually mapped onto the surface of a sphere. This transformation is unique and invertible, i.e. every point on the cortical surfaces corresponds to a single point on the sphere and vice versa (a property mathematicians call an isomorphism). Moreover, the neighborhood relation between points, i.e. the topology, is preserved. Such a one to one mapping is possible because the spherical and the cortical surfaces are both singly connected and therefore topologically equivalent. For each cortical hemisphere *Freesurfer* creates files containing the vertex coordinates (of about 100,000 vertices) and the corresponding tessellation (of about 200,000 triangles) for the gray-white matter boundary, the boundary between the gray matter and the cerebral spinal fluid, the spherical surface, and surfaces from inflation steps as desired. The tessellation for all of these surfaces is the same and every point on the sphere has a unique partner on all the other surfaces. This allows for a parameterization which maps the 3-dimensional cartesian coordinates (x, y, z) of the vertices for each surface onto two angles, the latitude ψ and longitude φ on the sphere. In other words, for each pair of angles (ψ, φ) there exists a triple of coordinates (x, y, z), which corresponds to a point located on a cortical or inflated surface. An example for the color coded x-, y- and z-coordinates of the gray-white matter boundary is shown in fig. 3 (top row) with φ running along the horizontal axis and ψ running vertically. The middle row shows a representation of the same quantities in polar coordinates where ψ runs in the radial and φ in the azimuthal direction. Contour lines for constant values of x, y and z (indicated in green) represent the surface in sagittal, coronal and axial slices, respectively, as shown in the bottom row.

Such a parameterization in spherical coordinates also allows for defining a coordinate system on the folded surfaces as shown in fig. 4. Such a coordinate system is useful for visualization purposes and for comparisons between different subjects [19], [20].

3 The Dataset

Throughout this chapter we will use a dataset that simulates an MEG experiment where sources are active at two locations along the anterior and posterior wall of the central sulcus pointing into a direction perpendicular to the gray-white matter boundary as shown in fig. 5.

We assume the time courses of activity at these locations to be damped oscillations plotted in the inserts, where the red curve is a time shifted version of the time series plotted in blue. We further assume that we measure the gradient of the radial component of the magnetic field at locations derived from a CTF Omega-151 magnetometer system (VSM MedTech Ltd., Port Coquitlam, BC, Canada), by calculating the superposition of magnetic fields form the individual six dipoles using the formula by Sarvas [15], which implicitly

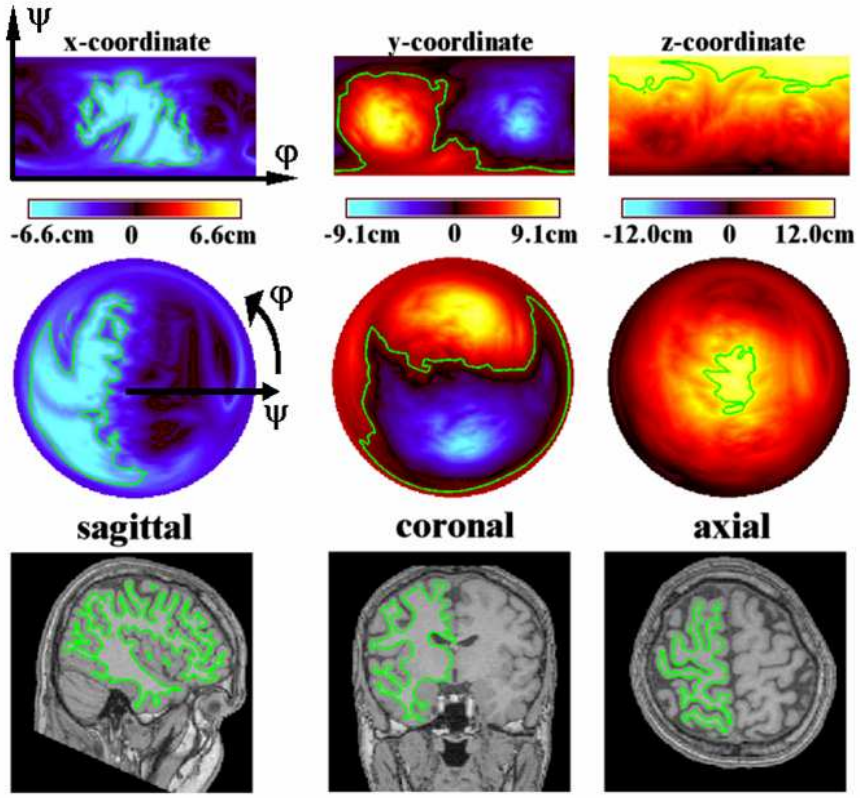

Fig. 3. Parameterization of the cortical surface. The x-, y- and z-coordinates of the folded three dimensional surface are expressed as continuous functions of the variables ψ and φ.

takes the contributions from the induced secondary currents in a spherical conducting volume into account.

$$\mathbf{B}(\mathbf{r}) = \frac{\mu_0}{4\pi F^2(\mathbf{r}, \mathbf{r_q})} \{F(\mathbf{r}, \mathbf{r_q})\, \mathbf{q} \times \mathbf{r_q} - [(\mathbf{q} \times \mathbf{r_q}) \cdot \mathbf{r}]\, \nabla F(\mathbf{r}, \mathbf{r_q})\} \tag{7}$$

where $\mathbf{r}$ denotes the location where the field is measured and $\mathbf{r_q}$ is the location of the dipolar current source with direction $\mathbf{q}$. The scalar function $F(\mathbf{r}, \mathbf{r_q})$ and its gradient $\nabla F(\mathbf{r}, \mathbf{r_q})$ are explicitly given by

$$\begin{aligned} F(\mathbf{r}, \mathbf{r_q}) &= d\,(r\,d + r^2 - \mathbf{r_q} \cdot \mathbf{r}) \\ \nabla F(\mathbf{r}, \mathbf{r_q}) &= \{\frac{d^2}{r} + \frac{\mathbf{d} \cdot \mathbf{r}}{d} + 2(d + r)\}\, \mathbf{r} - \{d + 2r + \frac{\mathbf{d} \cdot \mathbf{r}}{d}\}\, \mathbf{r_q} \end{aligned} \tag{8}$$

where the abbreviations $\mathbf{d} = \mathbf{r} - \mathbf{r_q}$, $d = |\,\mathbf{d}\,|$ and $r = |\,\mathbf{r}\,|$ have been used.

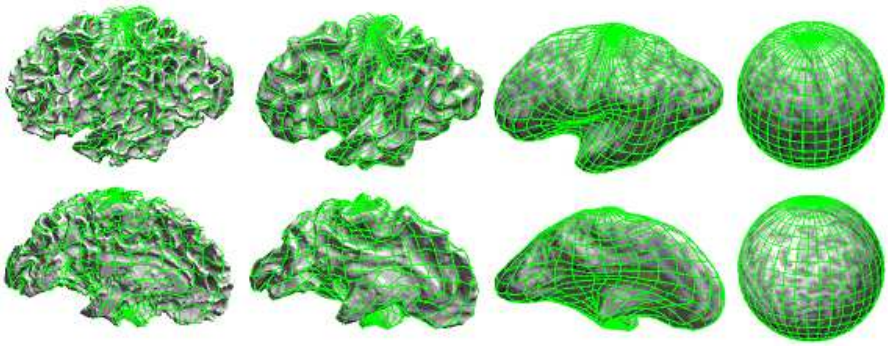

Fig. 4. Inflation steps of the cortical surface into a sphere. Because of the topological equivalence between the folded surfaces and the inflated sphere, the spherical coordinate system can be mapped back onto the cortical surface.

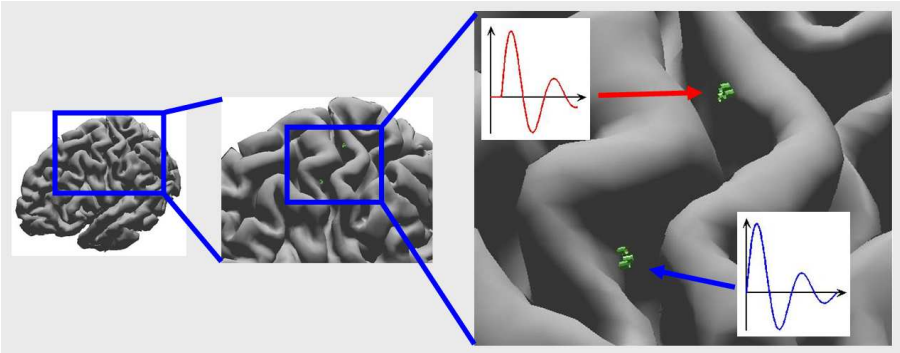

Fig. 5. Sources at two locations along the anterior and posterior wall of the central sulcus pointing into a direction perpendicular to the gray-white matter boundary. The red and blue curves in the inserts represent the time course of neural activity in these regions.

The signal that is picked up by a sensing coil is given by the scalar product of the vector of the magnetic field and the normal vector of the coil area. A first order gradient is simulated by subtracting the signal measured at the outer coil from the signal picked up by the inner coil. In addition to the deterministic activity from the sources in the two active regions in the central sulcus two kinds of noise are added. First, to the sources themselves, and second to 500 locations on the cortical surface that are randomly chosen at each of the simulated 100 time steps. This way a total of 200 'trials' are created. Plots of the average time series across trials in a topological layout of the sensors as well as the spatial patterns at 20 points in time that would be measured in the given scenario are shown in fig. 6 and fig. 7, respectively.

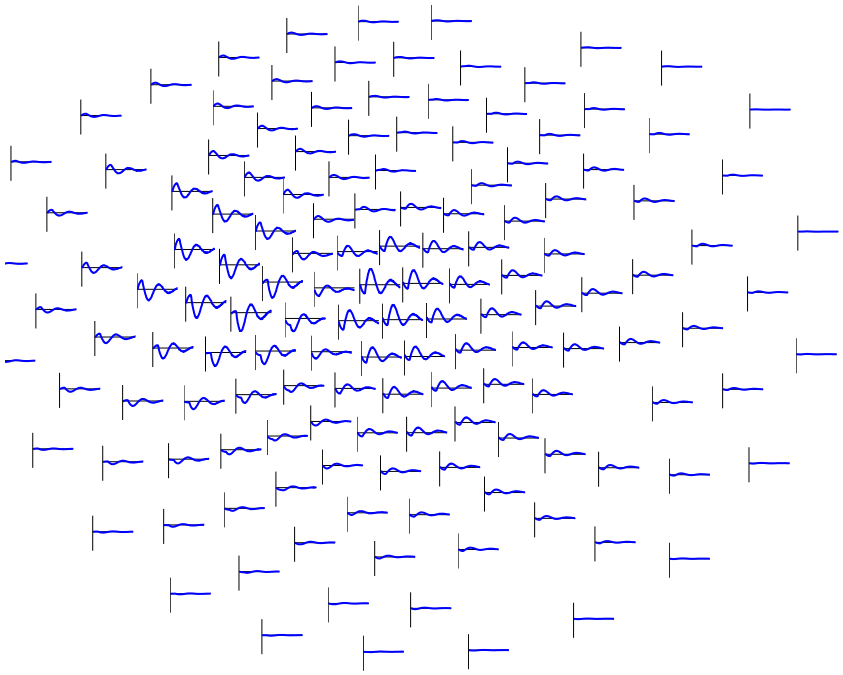

Fig. 6. Time series of the simulated data at 144 spatial locations, assuming that 7 of the 151 sensors were broken. Sensors are shown in polar projections with the nose on top.

4 Beamforming

4.1 The Basics

The basic idea behind beamforming in human brain research is to estimate the time course $q(t)$ of a current dipole at location $\mathbf{r}$ and direction $\mathbf{d}$ given measurements of one or more components of the magnetic field along a surface outside the head (MEG) or/and the electric potential on the scalp surface (EEG). We assume that we have recordings from M different sensor locations taken within a time span T and lumped together to a vector $\mathbf{H}(t)$ representing the measured signal. The goal is to find a set of filter coefficients $\mathbf{w}$ such that the relation

$$q(t) = \mathbf{w} \cdot \mathbf{H}(t) \tag{9}$$

is fulfilled. The components of $\mathbf{w}$ are called the beamformer weights and are determined by minimizing the source power P over a time span T while keeping the projected signal constant $\mathbf{w} \cdot \mathbf{L} = 1$, where $\mathbf{L}$ is the forward solution or lead field [12] of a unit source located at $\mathbf{r}$ with direction $\mathbf{d}$. The (average) source power can be expressed as

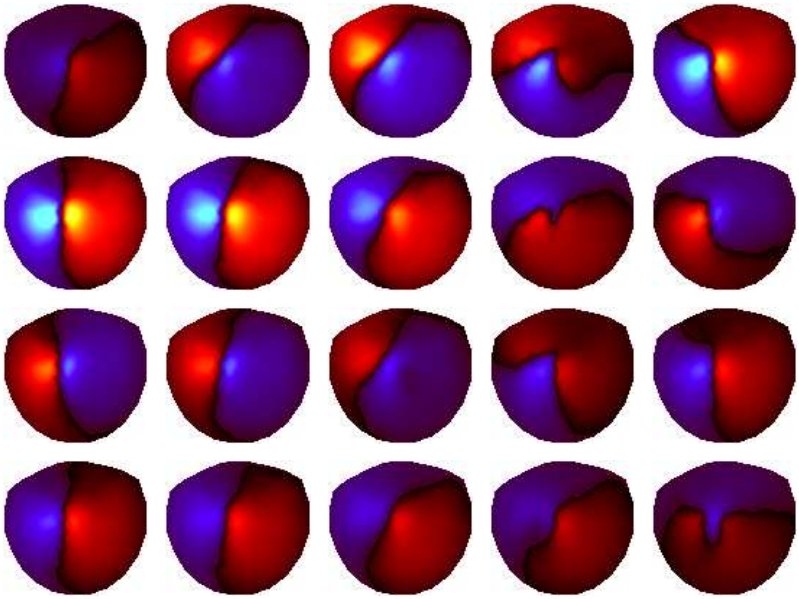

Fig. 7. Spatial patterns at 20 time points from top left to bottom right.

$$P = \frac{1}{T}\int_0^T q^2(t)\,dt = \frac{1}{T}\int_0^T \{\mathbf{w}\cdot\mathbf{H}(t)\}^2\,dt = \mathbf{w}\cdot\boldsymbol{C}\,\mathbf{w} \tag{10}$$

where $\boldsymbol{C}$ represents the correlation matrix $C_{ij} = \frac{1}{T}\int_0^T H_i(t)\,H_j(t)\,dt$.

The details on how to deal with such a minimization under constraints are described in appendix A where the beamforming vector $\mathbf{w}$ is explicitly derived as

$$\mathbf{w} = \frac{\boldsymbol{C}^{-1}\,\mathbf{L}}{\mathbf{L}\cdot\boldsymbol{C}^{-1}\,\mathbf{L}} \tag{11}$$

and where it is also shown that the source power P can be written in the form

$$P = \mathbf{w}\cdot\boldsymbol{C}\,\mathbf{w} = \{\mathbf{L}\cdot\boldsymbol{C}^{-1}\,\mathbf{L}\}^{-1} \tag{12}$$

As pointed out by Huang et al. [13] the expression for the beamformer weights (11) and the global source power (12) are the same for all so-called linearly constrained minimum variance beamformers (LCMV) that exist in the literature. The differences between them are essentially threefold: First, in the way two quantities called the global and time dependent neural activity index are calculated. The global neural activation is a measure of activation in brain areas over a certain time span. The time dependent neural activity index is a time series representing local activations and is most meaningful at

locations where the global index is large. The beamformers differ in the way these quantities are normalized, an issue originating from the inhomogeneous sensitivity of the beamformers with respect to depth and direction of the sources. An extreme case is MEG which is virtually blind to dipoles with a radial direction[2].

The second difference is how the beamformers treat low dimensional signals, i.e. signals with a low noise level like averages, where the correlation matrix $\boldsymbol{C}$ is singular and does not have an inverse. This problem can be dealt with by either subspace projection or regularization. The former reduces the dimensionality to the subspace defined by the eigenvectors of the correlation matrix which correspond to eigenvalues that are significantly bigger than zero. The latter is performed by adding a constant (representing uncorrelated noise) to the diagonal of the correlation matrix while keeping its original dimension. Both techniques, as discussed in detail in the following section, lead to matrices that are invertible. Explicit expressions for the global and time dependent neural activity index for the different types of beamformers found in the literature as distinguished by Huang et al. [13] are given in table 1.

Type	Global activity index	Time dependent activity index	Ref.
I	$N_a = \frac{\{\mathbf{L}\cdot\boldsymbol{C}^{-1}\mathbf{L}\}^{-1}}{\{\mathbf{L}\cdot\boldsymbol{\Sigma}^{-1}\mathbf{L}\}^{-1}} = \frac{\mathbf{L}\cdot\boldsymbol{\Sigma}^{-1}\mathbf{L}}{\mathbf{L}\cdot\boldsymbol{C}^{-1}\mathbf{L}}$	$n_a(t) = \frac{q^2(t)}{\{\mathbf{L}\cdot\boldsymbol{\Sigma}^{-1}\mathbf{L}\}^{-1}} = \frac{\{\mathbf{w}\cdot\mathbf{H}(t)\}^2}{\{\mathbf{L}\cdot\boldsymbol{C}^{-1}\mathbf{L}\}^{-1}}$	[5]
II	$N_a = \frac{\mathbf{w}\cdot\boldsymbol{C}\,\mathbf{w}}{\lvert\mathbf{w}\rvert^2} = \frac{\mathbf{L}\cdot\boldsymbol{C}^{-1}\mathbf{L}}{\mathbf{L}\cdot\boldsymbol{C}^{-2}\mathbf{L}}$	$n_a(t) = \frac{\{\mathbf{w}\cdot\mathbf{H}(t)\}^2}{\lvert\mathbf{w}\rvert^2} = \frac{\{\mathbf{L}\cdot\boldsymbol{C}^{-1}\,\mathbf{H}(t)\}^2}{\mathbf{L}\cdot\boldsymbol{C}^{-2}\,\mathbf{L}}$	[2], [14]
III	$N_a = \frac{\mathbf{w}\cdot\boldsymbol{C}\,\mathbf{w}}{\mathbf{w}\cdot\boldsymbol{\Sigma}\,\mathbf{w}} = \frac{\mathbf{L}\cdot\boldsymbol{C}^{-1}\mathbf{L}}{\mathbf{L}\cdot\boldsymbol{C}^{-1}\,\boldsymbol{\Sigma}\,\boldsymbol{C}^{-1}\,\mathbf{L}}$	$n_a(t) = \frac{\{\mathbf{w}\cdot\mathbf{H}(t)\}^2}{\mathbf{w}\cdot\boldsymbol{\Sigma}\,\mathbf{w}} = \frac{\{\mathbf{L}\cdot\boldsymbol{C}^{-1}\,\mathbf{H}(t)\}^2}{\mathbf{L}\cdot\boldsymbol{C}^{-1}\,\boldsymbol{\Sigma}\,\boldsymbol{C}^{-1}\,\mathbf{L}}$	[6]
IV	$N_a = \frac{\{\mathbf{L}\cdot\boldsymbol{C}^{-n}\,\mathbf{L}\}^{-1}}{\{\mathbf{L}\cdot\boldsymbol{\Sigma}^{-n}\,\mathbf{L}\}^{-1}} = \frac{\mathbf{L}\cdot\boldsymbol{\Sigma}^{-n}\,\mathbf{L}}{\mathbf{L}\cdot\boldsymbol{C}^{-n}\,\mathbf{L}}$	$n_a(t) = \frac{\mathbf{w}\cdot\{\mathbf{H}(t)\cdot\mathbf{H}(t)\}^n\mathbf{w}}{\mathbf{L}\cdot\boldsymbol{\Sigma}^{-n}\,\mathbf{L}} = \frac{\lvert\mathbf{H}(t)\rvert^{2n}\lvert\mathbf{w}\rvert^2}{\mathbf{L}\cdot\boldsymbol{\Sigma}^{-n}\,\mathbf{L}}$	[13]

Table 1. Classification of the global neural activity index N_a and the time-dependent index $n_a(t)$ according to Huang et al. [13]. Here $\mathbf{L}$ represents the lead field, $\mathbf{H}(t)$ is the signal measured at the sensor locations, $\mathbf{w}$ the beamforming filter, $\boldsymbol{C}$ is the covariance matrix of the signal at the times of interest and $\boldsymbol{\Sigma}$ the covariance matrix of the noise. $\boldsymbol{\Sigma}$ is either estimated from baseline data or chosen as a constant times the identity matrix.

The third difference between the linearly constrained minimum variance beamformers concerns the way the underlaying brain volume is scanned. There

[2] It should be pointed out that this is not due to technological limitations and also has nothing to do with the fact that the CTF system we are using here measures mainly the radial component of the field. The reason is that a radial current in a spherical conductor does not produce any magnetic field outside the sphere which can be easily seen in the formula by Sarvas (7). As the direction of any radial current $\mathbf{q}$ is parallel to the position vector $\mathbf{r_q}$, their vector product is equal to $\mathbf{0}$, which implies $\mathbf{B}(\mathbf{r}) = \mathbf{0}$.

are essentially three procedures to estimate the neural activity inside the brain. First there is vector beamforming: the volume is divided into voxels of a certain size (typically cubes with a side length of a few millimeters) and the global neural activity index for the center of each voxel is calculated three times for unit sources pointing into the x-, y- and z-direction. This way not only the activity is detected but also the direction of the source can be found. There are drawbacks using this method particularly with MEG, which is insensitive to radial currents, and therefore the estimate of a vector with a strong radial component is prone to large errors. This problem with radial components is avoided in the procedure introduced by Robinson and Vrba [6] known in the literature as SAM (Synthetic Aperture Magnetometry). For this procedure within each voxel only tangential dipole directions are scanned and the direction showing the largest activity is used. It is this search in the tangential plane, which is different for every voxel as opposed to the fixed three components of the vector beamformers that has led some authors to call SAM a nonlinear procedure [16]. The third possibility to define locations and directions of potential sources, which we will use for demonstrating beamformers' performances later in this chapter, is to apply anatomical constraints where the currents are restricted to the cortical gray matter with a direction perpendicular to the gray-white matter boundary. This constraint is motivated by the fact that gray matter is organized in macrocolumns of pyramidal cells that act coherently to build assemblies of $10^4 - 10^5$ simultaneously active neurons which are necessary to produce a signal strong enough that it can be picked up by MEG sensors or EEG electrodes. The disadvantage here is the need for high-resolution structural MRIs from all subjects that are well coregistered with the sensor or electrode locations.

4.2 Beamformer Performance: Regularization and Subspace Expansion

Independent of which one of the beamformer types is used it is always necessary to obtain the inverse of the covariance matrix[3] $\boldsymbol{C}$. An inverse may not exist or its computation can be numerically unstable if $\boldsymbol{C}$ is close to singular which happens if the signal space has a dimension smaller than the number of sensors. In a covariance matrix calculated from averaged signals, for instance, there are typically only a few eigenvalues that are significantly different from zero and the matrix is at least numerically singular. As mentioned above there exist two ways to work around this problem called regularization and subspace projection.

[3] The covariance matrix is the correlation matrix scaled such that the sum of all its eigenvalues is equal to 1. As we give numerical values for the regularization parameters this is a more appropriate representation than the correlation matrix, since the values in the covariance matrix do not depend on the units the magnetic field is measured in.

In regularization a constant σ is added to the diagonal of the covariance matrix in order to create a non-singular matrix. The effects of regularization are shown in fig. 8 for both the global and time dependent neural activity index calculated from the dataset described previously using a beamformer of type III. In contrast to Huang et al.'s version given in the table, we will not use the square in the numerator for the time dependent activity index in order to preserve direction of current flow. The global activity index is color-coded from red to yellow and thresholded at the same level for all four plots at 30% of its maximum. The inserts show the time series (solid) representing the time dependent activity index on top left in red for the active region in the posterior wall of the central sulcus and on bottom right in blue for the source in the anterior wall. The dashed lines in the inserts represent the ideal response.

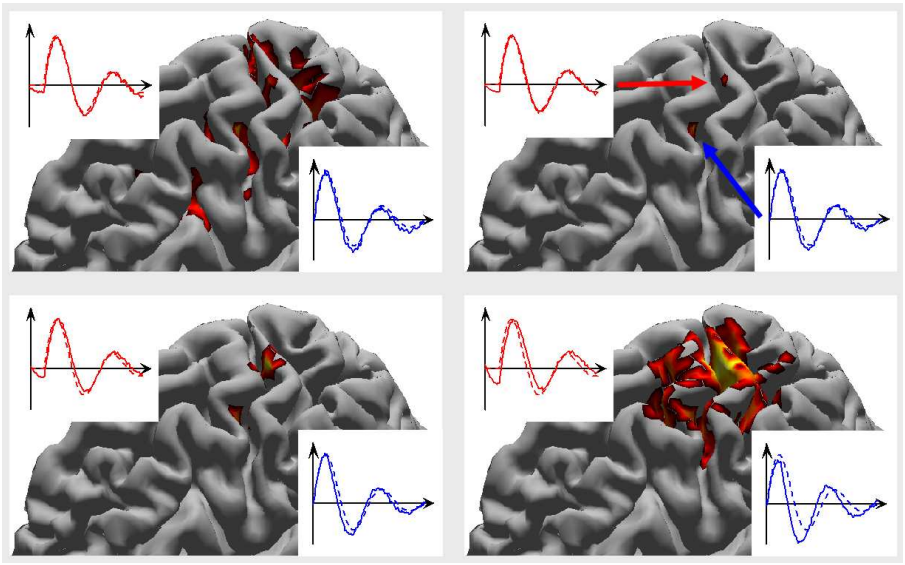

Fig. 8. Global neural activity index on the cortical surface for four different regularizations calculated from a beamformer of type III. From left top to right bottom the regularization parameter σ is increased from $5{\times}10^{-4}$ to 0.5 by factors of 10. On the top left the regularization parameter is too small and numerical instabilities distort the beamformer performance. In the bottom row σ is too big, the beamformer becomes less focussed or even blurred and activity from other regions leaks into the locations of interest. Inserts show the time dependent index reconstructed at the regions of maximum activity (solid) and the ideal curve (dashed). Especially on the bottom right a phase shift between these curves can be seen that originates from leakage of activity between the two regions due to a lack of focus.

In the top left plot a regularization parameter of $\sigma = 5 \times 10^{-4}$ is used. The time series for the time dependent activity index are in good agreement with the ideal shape, but the global index shows activity in many regions where no source is present. The determinant of the covariance matrix in this case is too small so that numerical errors prevent the calculation of a correct inverse. In the plot on the top right the regularization is $\sigma = 5 \times 10^{-3}$ and the matrix is well regularized. The time series overlap well with the ideal curves and the global activity index is focused and localized at the correct spots. In the lower left σ is 0.05. The spots of activity become slightly blurred and the time series start to show a phase shift with respect to the ideal functions indicating a superposition of the two original curves. These effects are even more pronounced on the bottom right with $\sigma = 0.5$, where over-regularization is obvious: the activity is blurred over wide regions and the time dependent index is clearly shifted, i.e. we obtain superpositions of the two time series. In short, if the regularization parameter is too small numerical instabilities distort the beamformer performance, if σ is too big the beamformer becomes less focussed or even blurred and activity from other regions leaks into the locations of interest. Unfortunately, σ is not known upfront and needs to be determined by trial and error.

The subspace projection is done by using the subspace defined by the eigenvectors of the covariance matrix whose corresponding eigenvalues are sufficiently different from zero. Subspace expansion of the type III beamformer is shown in appendix A and the beamformer weights and the neural activity indices with the proper normalizations turn out to be

$$\begin{aligned} \mathbf{w} &= \sum_{k=1}^{N} \frac{\{\mathbf{L} \cdot \mathbf{v}^{(k)}\}^2}{\lambda^{(k)}} \{\sum_{n=1}^{N} \frac{\{\mathbf{L} \cdot \mathbf{v}^{(n)}\}^2}{\lambda^{(n)}}\}^{-1} \mathbf{v}^{(k)} \\ N_a &= \frac{\sum_{n=1}^{N} \{\mathbf{L} \cdot \mathbf{v}^{(n)}\}^2}{\sum_{n=1}^{N} \frac{\{\mathbf{L} \cdot \mathbf{v}^{(n)}\}^2}{\lambda^{(n)}}} \\ n_a(t) &= \frac{\mathbf{w} \cdot \mathbf{H}(t)}{|\,\mathbf{w}\,|} \end{aligned} \tag{13}$$

where $\lambda^{(n)}$ and $\mathbf{v}^{(n)}$ are the eigenvalues and eigenvectors of the covariance matrix, respectively.

Figure 9 shows the effects of subspace projection when taking different numbers of eigenvalues and eigenvectors into account. Specifically, starting at the top left to bottom right these numbers are 4, 8, 12 and 50, respectively. The global activity index is blurred if not enough dimensions are taken into account and gets more focused as this number increases. On the other hand, if too many dimensions are used the time dependent index becomes contaminated by noise.

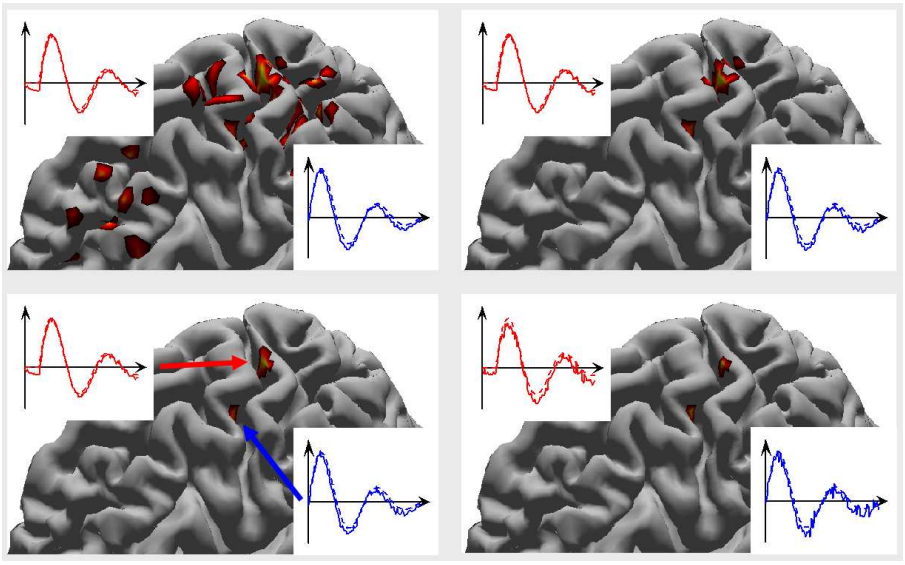

Fig. 9. Global neural activity index on the cortical surface for four different subspace dimensions calculated from a beamformer using (13). From top left to bottom right the subspace dimensions are 4, 8, 12 and 50, respectively. The global activity index is blurred if not enough dimensions are taken into account and gets more focused as this number increases. On the other hand, if too many dimensions are used the time dependent index becomes contaminated by noise.

5 Coherence and Granger Causality

Statistical measures have been used for a long time to study synchronization and desynchronization in higher frequency bands in datasets from EEG/MEG recordings (see e.g. [21]) and measurements of the local field potential from implanted electrodes [22]. Here we will establish coherence and Granger causality obtained from the time dependent neural activity index of the two active regions on the cortical surface as measures that allow for detecting connections between different brain regions or functional brain connectivity in general. We will briefly describe how these quantities are defined and calculated, and refer the reader to the chapter by Kaminski (this volume) for more detailed discussions on related topics.

5.1 Coherence

Coherence is calculated starting from two time series $x(t)$ and $y(t)$ and obtaining their Fourier transforms

$$X(\omega) = \int_0^T x(t)\, e^{i\omega t}\, dt \qquad \text{and} \qquad Y(\omega) = \int_0^T y(t)\, e^{i\omega t}\, dt \tag{14}$$

which leads to their spectral density functions

$$\begin{aligned} S_{xx}(\omega) &= \frac{1}{T}\,|\,X(\omega)\,|^2 \qquad S_{yy}(\omega) = \frac{1}{T}\,|\,Y(\omega)\,|^2 \\ S_{xy}(\omega) &= \frac{1}{T}\,X^*(\omega)\,Y(\omega) = S_{yx}(\omega) = \frac{1}{T}\,Y^*(\omega)\,X(\omega) \end{aligned} \tag{15}$$

From these functions the so-called squared coherence spectrum can be calculated as

$$C_{xy}(\omega) = \frac{|\,S_{xy}(\omega)\,|^2}{S_{xx}(\omega)\,S_{yy}(\omega)} \tag{16}$$

and we can define a global coherence as the integral of $C_{xy}(\omega)$ across all frequencies.

5.2 Granger Causality

From the coherence between two signals we can conclude whether they have an influence on each other. We cannot identify the direction, i.e. whether x drives y or y drives x, or whether there is mutual feedback between the two. A quantity which allows for such a distinction is a measure called Granger causality, where the word 'causality' in its name is a rather unlucky choice. Given two time series $x(t)$ and $y(t)$ we can never determine by any kind of analysis alone whether there is a causal relation between them, let alone who causes who. What Granger causality does allow to determine is whether the knowledge of one of the time series enables us to make a better prediction about the other one than would have been possible without that knowledge.

Granger causality is usually calculated from multivariate autoregressive models. To this end we assume that we have two time series x_t and y_t sampled at discrete[4] times t. Now we can set up autoregressive models for x_t and y_t, i.e. express their values at times t in terms of their past

$$x_t = \sum_{k=1}^{p} a_k\,x_{t-k} + \epsilon_t^{(x)} \qquad y_t = \sum_{k=1}^{p} c_k\,y_{t-k} + \epsilon_t^{(y)} \tag{17}$$

where we take p previous values of the time series into account to obtain a prediction of x_t and y_t. The equations in (17) are models of order p and the coefficients a_k and c_k have to be determined across all sequences in the time series. The difference between the predicted and the actual values for each x_t and y_t is given by the errors $\epsilon_t^{(x)}$ and $\epsilon_t^{(y)}$, respectively. Similarly we can set up multivariate autoregressive models where x_t does not only depend on its own past but also on previous values of y_t and vice versa

[4] We assume discrete time steps for simplicity, for continuous time series an embedding has to be determined, see Chen et al. [23] for details.

$$x_t = \sum_{k=1}^{p} a_k\, x_{t-k} + b_k\, y_{t-k} + \epsilon_t^{(x|y)} \qquad y_t = \sum_{k=1}^{p} c_k\, y_{t-k} + d_k\, x_{t-k} + \epsilon_t^{(y|x)} \quad (18)$$

We now say that y has a Granger causal influence on x if including y in the model for x on average improves the model, i.e. decreases the error

$$\frac{< \epsilon_t^{(x|y)} >}{< \epsilon_t^{(x)} >} < 1 \quad (19)$$

where $< \ldots >$ denotes the expectation value.

There are different ways to quantify the Granger causal influence of one time series onto another. One straightforward definition is evidently by means of the errors

$$g_{y \to x} = 1 - \frac{< \epsilon_t^{(x|y)} >}{< \epsilon_t^{(x)} >} \quad (20)$$

which is a number between zero and one with $g_{y \to x} = 0$ indicating that there is no influence.

5.3 Application to the Dataset

We applied the coherence measure and Granger causality to data sets that were constructed in the following way. A beamformer was separately applied to the 200 trials of simulated MEG data. Then the time series from each trial at the two active locations were extracted, the average time series was subtracted from each of the realizations and concatenated for each of the two regions. The time series corresponding to the red curve in fig. 5, we shall call $x(t)$, is a shifted version of the blue curve $y(t)$, which can be interpreted as originating from a one-directional coupling from the lower to the upper brain region with the finite distance between them leading to a time delay. We can vary the coupling strength between the two regions by gradually varying the second time series from random noise to $y(t)$. We therefore define a time series $y_c(t)$ as

$$y_c(t) = c\, y(t) + (1 - c)\, \xi(t) \qquad \text{with} \qquad 0 \leq c \leq 1 \quad (21)$$

where $\xi(t)$ represents gaussian white noise. Plots of coherence and Granger causality as functions of coupling strength c are shown in fig. 10. In the left plot the coherence between the two time series $x(t)$ and $y_c(t)$ increases with increasing coupling strength c. On the right, the line with squares represents the Granger causal influence $g_{y_c \to x}$ of $y_c(t)$ on $x(t)$ which also increases with coupling c, whereas $g_{x \to y_c}$ represented by the line with circles stays close to zero independent of c. We can therefore conclude that there is a one-directional connection between the two brain regions where the lower region feeds into the upper but not vice versa.

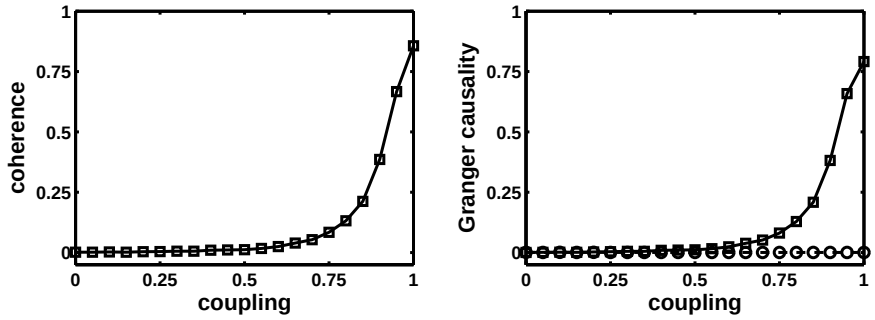

Fig. 10. Coherence (left) and Granger causality (right) as a function of the coupling strength between the two active regions. On the right, squares indicate a feed from the lower into the upper region whereas circles stand for a feed into the opposite direction. We can conclude that there is a one-directional connection between the two regions as the dashed line with circles stays close to zero for all couplings.

6 Conclusions and Outlook

Noninvasive recording of human brain activity has undergone a major change during the last decades with the development of high-density electrode and sensor grids in EEG and MEG, the introduction of MRI and functional MRI, and the explosion in computational power and storage capacity, representing one side of the coin: advances in technology. On the other side of this coin is written: "What do we get from all this stuff and how do we make sense of it?" How do we extract relevant information from a humongous tangled mass of data. Even though "relevant information" is a subjective matter that strongly depends on the specific questions one is interested in, relying on a single technology is in most cases not a good idea. In this chapter we have tried to show how different imaging technologies can be used to implement anatomical constraints on potential sources whose time series can then be identified from electrophysiological recordings and, moreover, give us insight regarding the existence and nature of a connection between two brain areas. There are other independent methods like Diffusion Tensor Imaging [24] or Structural Equation Modeling of functional MRI data [25] that can be used to probe connectivity, and only if different methods converge onto the same results can we have confidence that we have found something that really exists. In any case, there is no doubt that beamforming can become and probably will become one of the pillars that a future understanding of brain connectivity will be built on.

7 Acknowledgement

We thank Mingzhou Ding and Yonghong Chen for providing their Matlab code that was used to calculate coherence and Granger causality. Research supported by NINDS grant 1R01 NS48229.

A Minimizing the Source Power under Constraints

Here we show explicitly how the beamformer coefficients $\mathbf{w}$ and the source power P as given in (12) can be derived. Our starting point is a signal $\mathbf{H}(t)$ from EEG or MEG recordings where each of the M component $H^i(t)$ represents a time series from a single channel. Even though in practice these time series will be sampled at a finite rate we will treat time here as a continuous variable because the notation is less confusing that way. It is our goal to find a set of coefficients $\mathbf{w}_{\boldsymbol{\theta}}$ such that the sensor array becomes most sensitive to a current source at a certain location (x, y, z) and a certain direction (ϑ, φ) which we will abbreviate by $\boldsymbol{\theta} = \boldsymbol{\theta}(x, y, z, \vartheta, \varphi)$. Applying the beamformer $\mathbf{w}_{\boldsymbol{\theta}}$ to the signal $\mathbf{H}(t)$ we can write the global source power originating at $\boldsymbol{\theta}$ in the form

$$\begin{aligned} P_{\boldsymbol{\theta}} &= \tfrac{1}{T} \textstyle\int_0^T dt \, \{\mathbf{w}_{\boldsymbol{\theta}} \cdot \mathbf{H}(t)\}^2 \\ &= \tfrac{1}{T} \textstyle\int_0^T dt \, \sum_{i=1}^M \{w_\theta^i \, H^i(t)\}^2 \\ &= \textstyle\sum_{i=1}^M \sum_{j=1}^M w_\theta^i \, w_\theta^j \, \underbrace{\dfrac{1}{T} \displaystyle\int_0^T H^i(t) \, H^j(t) \, dt}_{C_{ij}} \end{aligned} \tag{22}$$

where C_{ij} represents the correlation matrix. Using $\boldsymbol{C}$, the global source power originating from $\boldsymbol{\theta}$ can now be written in the compact form

$$P_\theta = \sum_{i=1}^M \sum_{j=1}^M C_{ij} \, w_\theta^i \, w_\theta^j = \mathbf{w}_{\boldsymbol{\theta}} \cdot \boldsymbol{C} \, \mathbf{w}_{\boldsymbol{\theta}} \tag{23}$$

The goal of finding a vector $\mathbf{w}_{\boldsymbol{\theta}}$ such that the sensor array becomes most sensitive to a current source at $\boldsymbol{\theta}$ is achieved by minimizing the global power from all locations and directions while keeping the signal originating at $\boldsymbol{\theta}$ constant. In other words

$$P_{\boldsymbol{\theta}} = \mathbf{w}_{\boldsymbol{\theta}} \cdot \boldsymbol{C} \, \mathbf{w}_{\boldsymbol{\theta}} = \text{Min} \quad \text{with the constraint} \quad \mathbf{w}_{\boldsymbol{\theta}} \cdot \mathbf{L}_{\boldsymbol{\theta}} = 1 \tag{24}$$

where $\mathbf{L}_{\boldsymbol{\theta}}$ is the forward solution or lead field from a unit current source at $\boldsymbol{\theta}$. The constraint in (24) means that the components of $\mathbf{w}_{\boldsymbol{\theta}}$ cannot be varied independently in order to find the minimum but only combinations for

which the constraint is fulfilled are allowed. Without the constraint an obvious solution for the minimum would be $\mathbf{w}_{\boldsymbol{\theta}} \equiv \mathbf{0}$, which is certainly not what we are looking for, and it also violates the constraint.

The problem of finding the minimum under constraints of the form (24) is well known in physics and engineering, and can be solved using the method of Lagrange multipliers. The idea is to rewrite the constraint in the form

$$\mathbf{w}_{\boldsymbol{\theta}} \cdot \mathbf{L}_{\boldsymbol{\theta}} - 1 = 0 \tag{25}$$

where now the expression on the left hand side of (25) vanishes. It still vanishes if we multiply it by a constant λ, and it does not change anything if we add it to the global power we want to minimize, because we are essentially adding zero

$$P_{\boldsymbol{\theta}} = \sum_{i=1}^{M} \sum_{j=1}^{M} C_{ij}\, w_{\boldsymbol{\theta}}^{i}\, w_{\boldsymbol{\theta}}^{j} + \lambda \{ \sum_{i=1}^{M} w_{\boldsymbol{\theta}}^{i}\, L_{\boldsymbol{\theta}}^{i} - 1 \} = \mathrm{Min} \tag{26}$$

But now we can vary the components of $\mathbf{w}_{\boldsymbol{\theta}}$ independently and we find the minimum by taking the derivative of $P_{\boldsymbol{\theta}}$ with respect to $w_{\boldsymbol{\theta}}^{k}$ and solve

$$\frac{\partial P_{\boldsymbol{\theta}}}{\partial w_{\boldsymbol{\theta}}^{k}} = 2 \sum_{i=1}^{M} C_{ik}\, w_{\boldsymbol{\theta}}^{i} + \lambda\, L_{\boldsymbol{\theta}}^{k} = 0 \tag{27}$$

for $\mathbf{w}_{\boldsymbol{\theta}}$. If we rewrite (27) in matrix form

$$2\, \boldsymbol{C}\, \mathbf{w}_{\boldsymbol{\theta}} = -\lambda\, \mathbf{L}_{\boldsymbol{\theta}} \tag{28}$$

we find immediately

$$\mathbf{w}_{\boldsymbol{\theta}} = -\frac{\lambda}{2}\, \boldsymbol{C}^{-1}\, \mathbf{L}_{\boldsymbol{\theta}} \tag{29}$$

This solution still depends on the unknown Lagrange parameter λ, which can, however, be determined by inserting (29) into (25) leading to

$$\{ -\frac{\lambda}{2}\, \boldsymbol{C}^{-1}\, \mathbf{L}_{\boldsymbol{\theta}} \}\, \mathbf{L}_{\boldsymbol{\theta}} = 1 \quad \text{or} \quad \lambda = -2\, \{ \mathbf{L}_{\boldsymbol{\theta}} \cdot \boldsymbol{C}^{-1}\, \mathbf{L}_{\boldsymbol{\theta}} \}^{-1} \tag{30}$$

By inserting (30) into (29) we finally obtain for the beamformer coefficients

$$\mathbf{w}_{\boldsymbol{\theta}} = \frac{\boldsymbol{C}^{-1}\, \mathbf{L}_{\boldsymbol{\theta}}}{\mathbf{L}_{\boldsymbol{\theta}} \cdot \boldsymbol{C}^{-1}\, \mathbf{L}_{\boldsymbol{\theta}}} \tag{31}$$

and for the global source power

$$P_{\boldsymbol{\theta}} = \mathbf{w}_{\boldsymbol{\theta}} \cdot \boldsymbol{C}\, \mathbf{w}_{\boldsymbol{\theta}} = \{ \mathbf{L}_{\boldsymbol{\theta}} \cdot \boldsymbol{C}^{-1}\, \mathbf{L}_{\boldsymbol{\theta}} \}^{-1} \tag{32}$$

As mentioned previously, if the signal space is low-dimensional as for averaged signals for instance, the correlation matrix $\boldsymbol{C}$ is singular and does not

have an inverse. In this case a projection onto the relevant subspace can be achieved by expanding the beamformer vector $\mathbf{w}$ and the lead field $\mathbf{L}$ into the eigenvectors $\mathbf{v}^{(k)}$ of the correlation matrix that correspond to the N eigenvalues $\lambda^{(k)}$ that are significantly bigger than zero[5]

$$\mathbf{w} = \sum_{n=1}^{N} \omega_n \mathbf{v}^{(n)} \qquad \text{and} \qquad \mathbf{L} = \sum_{n=1}^{N} \zeta_n \mathbf{v}^{(n)} \tag{33}$$

Inserting (33) into (31) and (32) we obtain after straightforward calculations

$$\omega_k = \frac{\zeta_k}{\lambda^{(k)}} \{ \sum_{n=1}^{N} \frac{\zeta_n^2}{\lambda^{(n)}} \}^{-1} \qquad \text{and} \qquad P = \{ \sum_{n=1}^{N} \frac{\zeta_n^2}{\lambda^{(n)}} \}^{-1} \tag{34}$$

References

1. Frost III OL, (1972) An Algorithm for Linearly Adaptive Array Processing. Proc. IEEE 60:926–935
2. Borgiotti GV, Kaplan LJ (1979) Superresolution of Uncorrelated Interference Sources by Using Adaptive Array Techniques. IEEE Trans. Antennas Propagat. 27:842–845
3. Van Veen BD, Buckley KM (1988) Beamforming: A Versatile Approach to Spatial Filtering. IEEE ASSP Mag. 5:4–24
4. Sekihara K (1996) Generalized Wiener Estimation of Three-Dimensional Current Distribution from Biomagnetc Measurements. IEEE Trans. Biomed. Eng. 43:281–291
5. Van Veen BD, van Drongelen W, Yuchtman M, Suzuki A (1997) Localization of Brain Electrical Activity via Linearly Constraint Minimum Variance Spatial Filtering. IEEE Trans. Biomed. Eng. 44:867–880
6. Robinson SE, Vrba J (1999) Functinal neuroimaging by synthetic aperture magnetometry. In: *Recent advances in biomagnetism*, Yoshimito T, Kotani M, Kuriki S, Nagasato N, eds., Tohoku University Press, Sedai, Japan pp. 302–305.
7. Fuchs A (2002) Combining Technologies: The Use of Brain Surfaces. In: *Biomag 2002, Proc. 13th Int. Conf. on Biomagnetism*, Nowak H, Haueisen J, Geißler F, Huonker R, eds., VDE Verlag Berlin pp. 878–880
8. Hillebrand A, Barnes GR (2003) The use of anatomical constraints with MEG beamformers. Neuroimage 20:2302–2312
9. Abeles M (1991) *Corticonics: Neural Circuits of the Cerebral Cortex*, Cambridge University Press, Cambridge
10. Braitenberg V, Schüz A (1991) *Cortex: Statistics and Geometry of Neural Connectivity*, Springer, Berlin
11. Nunez PL (1981) *Electric Fields of the Brain*, Oxford University Press, Oxford
12. Moscher JC, Leahy RM, Lewis PS (1999) EEG and MEG Forward Solutions for Inverse Models. IEEE Trans. Biomed. Eng. 46:245–259

[5] As the correlation matrix is real, symmetric and positive semi-definite all eigenvalues are real and non-negative, and the eigenvectors are mutually orthogonal.

13. Huang M-X, Shih JJ, Lee RR, Harrington DL, Thoma RJ, Weisend MP, Hanion F, Paulson KM, Li T, Martin K, Miller GA, Canive JM (2004) Commonalities and Differences Among Vectorized Beamformers in Electromagnetic Source Imaging. Brain Topography 16:139–158
14. Sekihara K, Nagarajan SS, Poeppel D, Maranntz A, Miyashita Y (2001) Reconstructing Spatio-Temporal Activities of Neural Sources Using an MEG Vector Beamformer Technique. IEEE Trans. Biomed. Eng. 48:760–771
15. Sarvas J (1987) Basic mathematical and electromagnetic concepts of the biomagnetic inverse problem. Phys. Med. Biol. 32:11–22.
16. Vrba J, Robinson SE (2001) Differences between synthetic aperture magnetometry (SAM) and linear beamformers. In: *Biomag 2000, Proc. 12th Int. Conf. on Biomagnetism*, Nenonen J, Ilmoniemi RJ, Katila T, eds., Helsinki University of Technology, Espoo, Finland pp. 681-684.
17. Dale AM, Sereno MI (1993) Improved Location of Cortical Activity by Combining EEG and MEG with MRI Cortical Surface Reconstruction: A Linear Approach. Journal of Congnitive Neuroscience 5:162–176.
18. Dale AM, Fischl B, Sereno MI (1999) Cortical Surface-Based Analysis I: Segmentation and Surface Reconstruction. Neuroimage 9:179–194.
19. Fischl B, Sereno MI, Dale AM, (1999) Cortical Surface-Based Analysis II: Inflation Flattening and a Surface-Based Coordinate System. Neuroimage 9:194–207.
20. Fischl B, Sereno MI, Tootell RBH, Dale AM (1999) High-Resolution Intersubject Averaging and a Coordinate System for the Cortical Surface. Human Brain Mapping 8:272–284.
21. Pfurtscheller G, Lopes da Silva FH (1999) Event-related EEG/MEG synchronization and desynchronization: beasic principles. Clinical Neurophysiology 110:1842–1857
22. Brovelli A, Ding M, Ledberg A, Chen Y, Nakamura R, Bressler SL (2004) Beta oscillations in a large-scale sensorimotor cortical network: Directional influence revealed by Granger causality. PNAS 101:9849–9854.
23. Chen Y, Rangarajan G, Feng J, Ding M (2004) Ananlyzing Multiple Nonlinear Time Series with Extended Granger Causality. Phys. Lett. A 324:26–35
24. Westin CF, Maier SE, Mamata H, Nabavi A, Jolesz FA, Kikinis R (2002) Processing and visualization for diffusion tensor MRI. Medical Image Analysis 6:93–108
25. McIntosh AR, Gonzalez-Lima F (1994) Structural equation modeling and its application to network analysis in functional brain imaging. Human Brain Mapping 2:2–22.